Assessment and comparison of five satellite precipitation products in Australia

Assessment and comparison of five satellite precipitation products in Australia

Md. Atiqul Islam[a,*], Bofu Yu[b], and Nick Cartwright[a]

[a] *School of Engineering and Built Environment and Griffith Centre for Coastal Management, Griffith University, Gold Coast Campus, Queensland 4222, Australia*

[b] *School of Engineering and Built Environment and Australian Rivers Institute, Griffith University, Nathan Campus, Queensland 4111, Australia*

*Corresponding author:

Name: Md. Atiqul Islam

Email: atiqul.islam@griffithuni.edu.au, atiqul@ce.kuet.ac.bd

Address: School of Engineering and Built Environment, Griffith University, Gold Coast Campus, Parklands Drive, Queensland 4222, Australia, Telephone: +61755529142

Assessment and comparison of five satellite precipitation products in Australia

Quality satellite-derived precipitation products (SPPs) are needed for water resources inventories and management, particularly in poorly gauged regions around the world. The latest version of five SPPs were assessed against SILO (Scientific Information for Land Owners) gauge-based gridded precipitation dataset in Australia over a 5-year period from October 2014 to September 2019. The evaluation was carried out using a 0.50° grid at daily, seasonal, and annual temporal scales. The assessed SPPs were the Integrated Multi-satellitE Retrievals for GPM (Global Precipitation Measurement) (IMERG), TRMM (Tropical Rainfall Measuring Mission) Multi-satellite Precipitation Analysis (TMPA), Climate Prediction Centre (CPC) Morphing technique (CMORPH), Precipitation Estimation from Remotely Sensed Information using Artificial Neural Networks (PERSIANN), and PERSIANN-CDR (Climate Data Record). PERSIANN does not include any ground-based observations for bias-correction, while the other four products are bias-corrected against gauge-based data. Bias ratio and correlation coefficient for the five SPPs showed that the overall performance of IMERG and TMPA was better than that of CMORPH, PERSIANN, and PERSIANN-CDR for Australia. Seasonal analysis showed that IMERG had the better skill in winter. Overall, IMERG appeared to be the best SPP for Australia. However, TMPA also performed reasonably well, considering the climatological calibration implemented recently in the precipitation processing algorithm. The structural similarity index (SSI), a map comparison technique using a moving window-based approach, was used to compare similarities between a pair of gridded precipitation maps in terms of local mean, variance, and covariance. All the SPPs showed discrepancies in the spatial structure of the mean annual

precipitation, predominantly over some high precipitation areas in Australia. These local scale differences were not detectable in conventional cell by cell comparison or simply by visual inspection. Therefore, SSI could be an effective method to evaluate satellite precipitation estimation algorithm.

Keywords: Satellite precipitation products, GPM, TRMM, Australia, Structural Similarity Index

1. Introduction

Australia experiences a highly variable precipitation regime both in space and time, as the country has diverse climatic zones from the equatorial and tropical areas of the north, through the deserts of the western and central interior, to the temperate regions in the south. Precipitation over this driest inhabited continent on Earth plays a significant and critical role in dryland agriculture, groundwater recharge, domestic water supply, and healthy ecosystem functioning (Prosser 2011). Apart from these benefits, Australia is also prone to precipitation induced extreme hydroclimatic events, including floods, droughts, and occasional landslides (Sewell et al. 2016).

Reliable information on the amount, spatial distribution, and temporal variation of precipitation is essential for modelling of various environmental processes and for the development of water related resource and hazard management policies. In Australia, rain gauge stations are mostly concentrated in the populated coastal regions (Li and Shao 2010, Chappell et al. 2013). A significant portion of the Australian continent has very few or even no rain gauges, particularly in drier inlands (Chen et al. 2013). Further, rain gauge records are not always complete in space and time (Jeffrey et al. 2001). Inconsistencies and biases may occur due to different types of gauges,

methods of data recording, data processing and quality control for potentially erroneous values, and time of data recording among states and territories.

Whilst weather radars are capable of providing precipitation information with finer spatial and temporal scales, they mostly cover coastal areas in Australia and their vertical coverage is limited to below 3048 m above mean sea level (Bureau of Meteorology 2020). Radar precipitation products are also exposed to uncertainties because of inaccurate radar reflectivity-rain rate (Z-R) relationships according to the type of precipitation, beam blockages by complex terrain, signal attenuation, and bright band effects (Maggioni et al. 2016, Mei et al. 2014).

During the past two decades, the application of satellite-derived precipitation products (SPPs) has received notable attention for use in sparsely gauged and ungauged regions around the globe. SPPs have been adopted for various hydrometeorological applications, such as streamflow simulation (Xue et al. 2013), real-time flood forecasting (Li et al. 2015), drought monitoring (Vernimmen et al. 2012), landslide modelling (Rossi et al. 2017, Brunetti et al. 2018) as well as utilization in disease control framework (Schuster et al. 2011).

While numerous studies have been carried out around the world, only a limited number have focused on the evaluation of SPPs over Australia. Pipunic et al. (2015) investigated Tropical Rainfall Measuring Mission (TRMM) Multi-satellite Precipitation Analysis (TMPA) real-time products 3B42-RT version 7 (Huffman et al. 2007) against rain gauge observations for 1024 satellite pixels, nearly 9% of the land surface across mainland Australia. Most of the satellite pixels were located in the south-western, south-eastern, and eastern temperate climate zones of Australia. A very limited number of pixels were selected in the tropical and arid climate zones simply due to the sparse rain gauge network in these regions. Ebert et al. (2007) examined the 3B42-RT, Climate

Prediction Centre (CPC) Morphing technique (CMORPH) (Joyce et al. 2004), and Precipitation Estimation from Remotely Sensed Information using Artificial Neural Networks (PERSIANN) (Sorooshian et al. 2000) precipitation products against gauge-based interpolation estimates at the daily time scale. The study validated the older version of the products for a 5-year period from 2002 to 2006. Chen et al. (2013) evaluated gauge-adjusted TMPA data sets (3B42) with respect to gauge-based gridded reference estimates to capture tropical landfalls from 96 tropical cyclones passing over Australia during 1998-2011. Peña-Arancibia et al. (2013) also performed evaluation of 3B42 version 6, CMORPH, and PERSIANN precipitation estimates against gridded rain gauge data at a coarse spatial resolution (i.e. 1° × 1° latitude/longitude) over the south-western, south-eastern, eastern, and north-eastern parts of Australia. Pipunic et al. (2013) focused on a large arid basin (i.e. Lake Eyre basin) in Australia and validated 3B42 version 7, CMORPH, and PERSIANN using in-situ rain gauge data at only 24 locations.

In summary, previous studies have either focused on a particular region of interest and/or validated a limited number of SPPs. None of the studies has evaluated SPP algorithms across the different climate regimes of Australia. In addition, no attempt has been made to evaluate the latest SPP, derived from the Global Precipitation Measurement (GPM) mission, over Australia. The GPM mission first released data in March 2014 and has been shown to provide markedly improved precipitation estimates (Hou et al. 2014). Several studies from elsewhere in the world have reported that precipitation products of GPM show superior performance compared to TRMM precipitation products (Tan and Santo 2018, Tang et al. 2016, Xu et al. 2017).

In this study, Integrated Multi-satellitE Retrievals for GPM (IMERG) (Huffman et al. 2020, Huffman et al. 2019) with four other popular SPPs were selected to include

different types of satellite sensors i.e. infrared (IR) and passive microwave (PMW) as well as gauge-adjusted and non-adjusted products. This will facilitate quantification of the influence of these factors on SPP skill. Moreover, this study will uncover the strengths and limitations of the SPPs across diverse climate regions of Australia as the skill of these data sets varies in relation to precipitation type, climate, and topography (Pipunic et al. 2015). To explore the widest applicability and usage of the SPPs, the present analysis is carried out at daily, seasonal, and annual time scales.

For the first time, a novel spatial map comparison method, namely the structural similarity index (SSI), was applied to quantify the spatial distribution of the different SPPs in comparison with the gauge-based SILO (Scientific Information for Land Owners) dataset (Jeffrey et al. 2001). The SSI metric was originally developed to quantify the distortion of a compressed image from a reference image (Wang et al. 2004). More recently, SSI has been adapted for comparison of spatial ecological data (Wiederholt et al. 2019, Jones et al. 2016). However, SSI has not yet been applied for comparing spatial distribution of precipitation at different time scales. This SSI metric can identify local differences in the mean, variance, and spatial structure between two maps using a local neighbourhood-based approach.

The aim of the present study is to compare and evaluate the skill of five SPPs over the diverse climate zones of Australia against the daily gauge-based SILO dataset over a period of 5 years from October 2014 to September 2019. The specific objectives of this study include: (a) to assess the accuracy of the selected satellite precipitation products in terms of the bias and temporal correlation using cell by cell comparison, (b) to apply structural similarity index as a quality indicator in the context of comparing spatial distribution of the mean annual and seasonal precipitation, and (c) to rank the SPPs according to a multiple criteria set for application in Australia.

2. Study area and data

2.1. Study area

With an area of about 7.692 million km^2, Australia is the sixth largest country in the world, extending from 9° S-44° S and 112° E-154° E (see Figure 1(a)). Precipitation in Australia is influenced by large scale atmospheric and oceanic drivers (Risbey et al. 2009) and varies significantly across the country both spatially and temporally (King et al. 2014). The mean annual precipitation varies from less than 100 mm in central Australia to over 4000 mm in the wet tropics (Nicholls et al. 1997, Sivakumar et al. 2014). The driest part of Australia extends over the west coast of Western Australia (WA), north-eastern and central regions of South Australia (SA), and parts of Queensland (QLD), Northern territory (NT), and New South Wales (NSW) (Figure 1(a)). The northern part of the country (i.e. north-eastern WA, northern half of NT, and northern and north-eastern QLD) receives precipitation mostly during summer months from October through April. Monsoon depressions and tropical cyclones mainly bring precipitation over this region (King et al. 2014). The tropical east coast of QLD experiences the highest precipitation as the mountains are close to the coast (Figure 1(a)). South-western WA, south-eastern Australia, and western Tasmania (TAS) receive precipitation during the cooler months from April to November (Maher and Sherwood 2014). East coast lows also bring precipitation along the coast of NSW and Victoria (VIC) primarily in winter (King et al. 2014). The mountainous region of western TAS receives the highest precipitation during this season (Figure 1(a)). The mean annual precipitation ranges from over 2500 mm in the western coast of TAS to approximately 600 mm along the eastern coast (Grose et al. 2013).

Figure 1(b) shows six major precipitation zones of Australia based on precipitation amount in two contrasting seasons i.e. summer (November to April) and winter (May to October). Summer dominant zone has wet summer season and dry winter season. Conversely, winter dominant region receives precipitation in winter season and experiences dry summer season. Almost equal amount of precipitation is observed over the uniform zone both in summer and winter seasons while arid zone experiences low precipitation throughout the year.

2.2. SILO reference dataset

SILO, produced by the Queensland Department of Environment and Science, provides gridded precipitation data at 0.05° × 0.05° (latitude/longitude) spatial and daily temporal resolution across Australia since 1889 (Jeffrey et al. 2001). This precipitation product is derived via spatial interpolation of in-situ rain gauge measurements. SILO is updated when new records arrive, since precipitation observations are still provided in paper form for many locations throughout the country. The rain gauge observations are subject to routine error checking which ensures optimal quality of the interpolated precipitation estimates achievable based on the available in-situ observations. SILO dataset is produced using gauge precipitation data recorded according to local time at the place of observation. The precipitation total for a date is the amount of precipitation accumulated over a 24-h period from 9 am of the previous day (Jones et al. 2009).

2.3. SPPs

Each SPP has its own estimation algorithm that differs from others with respect to sensors of observation, technique of merging input datasets, and spatial and temporal scales of output data. A brief description of each product is given below, and some basic

spatiotemporal metadata of the selected SPPs is summarised in Table 1.

2.3.1. IMERG

The surface precipitation rate is derived from the Goddard Profiling (GPROF) algorithm and Precipitation Retrieval and Profiling Scheme (PRPS) using precipitation related PMW observations (Huffman et al. 2020, Huffman et al. 2019). These PMW estimates are gridded at 0.10° spatial and half-hourly time scale. The gridded PMW estimates are then intercalibrated using the Ku-band Combined Radar and Radiometer (CORRA) product as the reference. To overcome the limited sampling of PMW sensors, the CPC morphing technique is integrated in the IMERG algorithm to include IR estimates. The morphing algorithm was first introduced as the key component of CMORPH product (Joyce et al. 2004) and was further improved by incorporating a Kalman filter-based interpolation scheme to increase the accuracy of the product (Joyce and Xie 2011). IR precipitation data is estimated using IR brightness temperature from the PERSIANN Cloud Classification System (CCS) algorithm (Hong et al. 2004). In IMERG up through version 05 (V05), the morphing algorithm is implemented as follows: (1) motion vectors are computed from PMW-calibrated IR data, (2) PMW estimates are morphed using the motion vectors where enough PMW estimates are available, and (3) IR data is integrated with the propagated precipitation estimates via CMORPH-Kalman filter approach where PMW data are too sparse. From IMERG V06, numerical model variable i.e. total precipitable water vapour (TQV) from Modern Era-Retrospective Analysis for Research and Applications, Version 2 (MERRA-2) is used to derive motion vectors for final product (Tan et al. 2019). The merged PMW-IR satellite only precipitation products are bias-corrected against monthly gridded gauge-based datasets from Global Precipitation Climatology Centre (GPCC) to produce research grade

IMERG precipitation data. IMERG V06B Final run dataset (hereafter only IMERG) was downloaded from the website at https://disc.gsfc.nasa.gov/SSW/ for evaluation over the current study area.

2.3.2. TMPA

Before October 2014, research-quality TMPA products are computed in four steps: (1) the PMW precipitation estimates from different satellite sensors are intercalibrated and combined. First, all PMW sensors data are calibrated to TRMM Microwave Imager (TMI) and then adjusted to TRMM Combined Instrument (TCI) using TCI-TMI relationship (Huffman et al. 2010). The TCI-TMI calibration is established for each calendar month while TMI calibrations for different PMW sensors vary depending upon the individual sensor. Then, TCI estimate is selected in the 3-h time window for each 0.25° grid box if available. If not, TCI-adjusted sensors data are used. (2) PMW calibrated IR precipitation estimates are created. The PMW-IR calibration coefficients are calculated for each calendar month and are applied to each 3-h 0.25° IR grid box for that month (Huffman et al. 2010). (3) PMW and PMW calibrated IR precipitation products are combined in a way that PMW estimates are taken as it is when and where available and PMW-adjusted IR estimates are selected when PMW data are absent. (4) Finally, the multi-satellite PMW-IR merged 3-hourly precipitation estimates are summed over a calendar month (MS) and are combined with monthly gridded rain gauge data to produce monthly research-grade product 3B43 (SG). Now, the ratios of (monthly) SG/MS are computed for each 0.25° grid box and are applied to each 3-h precipitation field of the month, producing 3-hourly research quality product 3B42.

TCI data are not available due to the ultimate decommissioning of the TRMM Precipitation Radar (PR) after 7 October 2014 (Braun et al. 2014). To continue the

production of research grade TMPA data, climatological calibration is adopted in the same way as the real time (RT) version of TMPA i.e. 3B42-RT from October 2014. Since, TCI and rain gauge datasets are not available in real time, two-stage climatological calibration is employed to create 3B42-RT (Huffman et al. 2010). 14 years of data (1998-2011) is used to develop monthly (a) TCI-TMI relationship for providing TCI correction (described above in Step 1) and (b) 3B43-TCI adjustment for incorporating the mean of gauge data at the large scale (Huffman et al. 2010). It is noteworthy that 3B42-RT is not adjusted against monthly gauge data which is carried out for research grade products (described above in Step 4). However, climatologically calibrated 3B42 still includes gauge analysis as the precipitation product is produced about two months after the end of each month. This inclusion of gauge data overrides the 3B43-TCI adjustment described above in stage (b) of climatological calibration. The climatologically calibrated 3B42 dataset (hereafter only TMPA) is used in the present study. Consequently, to ensure homogeneity of the TMPA products, the present analysis commences in October 2014.

2.3.3. CMORPH

The latest version of CMORPH precipitation data with 1-h temporal and 0.25° spatial resolution were collected from the link: https://www.ncei.noaa.gov/data/cmorph-high-resolution-global-precipitation-estimates/access/. The CMORPH precipitation estimation algorithm integrates precipitation related data from various PMW sensors aboard low-Earth-orbiting (LEO) satellites. The PMW precipitation products of each sensor are calibrated against those from TMI (Xie et al. 2017). As TMI is switched off on 8 April 2015, climatological calibration is adopted after April 2015 for each month, for each 10° latitude band, and for land and ocean separately (Xie et al. 2017). The

TMI-adjusted PMW estimates from all sensors are combined taking only the one with the highest quality for each grid box. The daily snow cover map provided by the National Environmental Satellite, Data, and Information Service (NESDIS) is utilized to ensure the quality of the grid boxes covered by snow. In the meantime, motion vectors of precipitating clouds are derived from various geostationary-Earth-orbiting (GEO) satellites IR images (Joyce et al. 2004). Using motion vectors, the algorithm propagates combined PMW precipitation features from their respective measurement times to the target analysis time both in forward and backward directions. The raw CMORPH precipitation amounts are computed in space and time between two consecutive PMW observations by applying a time-weighted mean of the forward and backward propagated precipitation estimates. Hence, raw CMORPH determines the precipitation magnitudes using superior quality PMW estimates and employs the finer spatial and temporal resolution IR data indirectly. Finally, CPC daily gauge data is used to remove bias in the raw CMORPH data over land (Xie et al. 2017).

2.3.4. PERSIANN

PERSIANN precipitation products primarily relate IR observations of cloud-top brightness temperature (T_b) images with precipitation rates using a neural network technique (Hsu et al. 1997). Due to the high degree of uncertainty of the statistical relationships, the neural network model parameters are calibrated with PMW observations and are updated regularly as new precipitation estimates become available (Sorooshian et al. 2000). The current PERSIANN precipitation products with 0.25° × 0.25° latitude/longitude spatial and hourly temporal resolution were downloaded from the location at http://chrsdata.eng.uci.edu/.

2.3.5. PERSIANN-CDR

PERSIANN-CDR (Climate Data Record) algorithm is developed to create a consistent, long term, and high resolution SPP for climate studies. The product uses the historical archive of IR brightness temperature data from Gridded Satellite (GridSat-B1) in the International Satellite Cloud Climatology Project (ISCCP) (Ashouri et al. 2015). The PERSIANN algorithm is applied to the IR data to estimate 3-hourly precipitation rate at 0.25° spatial resolution (Hsu et al. 1997, Sorooshian et al. 2000). The nonlinear regression parameters of neural network model are trained and kept fixed during rain-rate estimation from IR data. The resulting precipitation products are resampled to 2.5° spatial and monthly time resolution and are bias-adjusted with Global Precipitation Climatology Project (GPCP) version 2.2 data (Adler et al. 2003). Lastly, the 3-hourly bias adjusted precipitation estimates are accumulated to produce daily PERSIANN-CDR data. It is worth mentioning here that PERSIANN-CDR algorithm does not incorporate any PMW data apart from monthly GPCP data in an indirect fashion (Ashouri et al. 2015). Due to its relatively long record length (1983-present), PERSIANN-CDR is a unique dataset compared to other contemporary SPPs. This dataset is particularly valuable for regions where ground-based precipitation observations are inadequate or absent for long-term precipitation climatology studies (e.g., to study trends and observed changes in the mean as well as the extreme precipitation events to develop reliable polices for water resources management).

3. SPP-SILO comparative analysis

3.1. Spatiotemporal discretisation

The daily accumulation time window of the SILO reference data which extends from 9

am to 9 am local time (i.e. 23:00:00 to 23:00:00 UTC (Coordinated Universal Time)) is used for the analysis as it is consistent with all SPPs except for TMPA and PERSIANN-CDR. The daily accumulation for TMPA runs from 22:30:00 to 22:30:00 UTC. For PERSIANN-CDR, the daily precipitation accumulation is between 00:00:00 and 24:00:00 UTC. Since, the analysis is performed at daily (24-h) time scale, it is assumed that the 0.5 h and 1.0 h offset times for TMPA and PERSIANN-CDR respectively, will not affect the results significantly. The comparative analysis was conducted over the time slice from October 2014-September 2019 to ensure the time homogeneity of the TMPA product whose processing algorithm underwent significant change in October 2014 (see section 2.3.2).

The IMERG and SILO products are available at 0.10° and 0.05° spatial resolutions respectively, while all other SPPs have identical spatial resolution of 0.25°. For the comparison, all SPPs and SILO dataset were spatially averaged on to a 0.50° × 0.50° analysis grid. To remap IMERG at 0.25° scale, it is necessary to apply an interpolation technique. The present analysis considered 0.50° scale to avoid the effect of interpolation on precipitation estimates.

3.2. Conventional skill metrics

To assess the skills of the SPPs, bias ratio (BR) and correlation coefficient (CC) are computed at each grid location across the country for the study period.

- BR indicates the ratio of SPP to the SILO value. The perfect score of BR is 1 while overestimation and underestimation will lead to values greater than 1 and less than 1, respectively.
- CC is applied to quantify the linear relationship between SPPs and SILO dataset. CC score varies between -1 and +1. CC value of +1 represents that

SPPs have perfect positive correlation with SILO whereas -1 denotes perfect negative correlation. If CC value is 0, there is no linear relationship between SPP and SILO. BR and CC are expressed as follows:

$$\mathrm{BR} = \frac{\sum_{i=1}^{N} P_{\mathrm{S}_i}}{\sum_{i=1}^{N} P_{\mathrm{G}_i}} \tag{1}$$

$$\mathrm{CC} = \frac{\sum_{i=1}^{N}(P_{\mathrm{S}} - \overline{P_{\mathrm{S}}})(P_{\mathrm{G}} - \overline{P_{\mathrm{G}}})}{\sqrt{\sum_{i=1}^{N}(P_{\mathrm{S}} - \overline{P_{\mathrm{S}}})^2}\sqrt{\sum_{i=1}^{N}(P_{\mathrm{G}} - \overline{P_{\mathrm{G}}})^2}} \tag{2}$$

where $P_{\mathrm{S}}(= P_{\mathrm{S}_i})$ is the SPP value for the ith day, $P_{\mathrm{G}}(= P_{\mathrm{G}_i})$ is the SILO precipitation value for the ith day, and N is the number of daily precipitation event at each pixel location. $\overline{P_{\mathrm{S}}}$ and $\overline{P_{\mathrm{G}}}$ show the mean SPP and SILO precipitation amount, respectively for the N number of daily events over each grid box.

All Australia mean and standard deviation (STD) of BR and CC are also computed for each SPP. Mean and STD of BR are calculated using Z where Z is estimated as follows:

$$Z = \begin{cases} \mathrm{BR}, & \mathrm{BR} \geq 1 \\ 1/\mathrm{BR}, & \mathrm{BR} < 1 \end{cases} \tag{3}$$

The lower the Z value and the higher the CC value, the better the skill of the SPP. For the standard deviation, the lower the STD value, the smaller the spread among all grid boxes, the better the skill of the SPP because of spatial consistency.

3.3. SSI

As discussed previously, the SSI was initially developed for image analysis and has been applied to investigate spatial patterns in the field of ecology (Jones et al. 2016,

Wiederholt et al. 2019). This method to compare the precipitation maps at seasonal and annual time scales was applied to SPPs for the first time based on the literature. The method compares the value of each cell between SPP and SILO and considers the values of the neighbouring cells at the same time. For each cell, a locally moving window is used to include n numbers of neighbouring cells. An equal amount of weight (w_j) is given to each of the neighbouring cells so that $\sum_{j=1}^{n} w_j = 1$. The size of the window is user-defined and has the lower limit of 3 × 3 cells which was adopted in this study, in order to provide information on more local differences between SPP and SILO. For two matrices representing gridded maps, the similarity in the mean (SIM), the variance (SIV), and the pattern or covariance (SIP) were estimated using the following equations (Jones et al. 2016, Wiederholt et al. 2019):

$$\mathrm{SIM}(S,G) = \frac{2\mu_s\mu_g + c_1}{\mu_s^2 + \mu_g^2 + c_1} \tag{4}$$

$$\mathrm{SIV}(S,G) = \frac{2\sigma_s\sigma_g + c_2}{\sigma_s^2 + \sigma_g^2 + c_2} \tag{5}$$

$$\mathrm{SIP}(S,G) = \frac{\sigma_{sg} + c_3}{\sigma_s\sigma_g + c_3} \tag{6}$$

In the above equations, subscripts s and g represent values for maps S (SPP) and G (SILO), respectively. Three constants c_1, c_2, and c_3 were used to ensure numerical stability of these equations when the denominator value of the equations is close to zero. The values of these constants were calculated using the range (R) of the values of the maps being compared and two constants, $k_1 = 0.01$ and $k_2 = 0.03$. Thus, $c_1 = (k_1R)^2$, $c_2 = (k_2R)^2$, and $c_3 = \frac{c_2}{2}$. Meanwhile, μ_s (μ_g), σ_s^2 (σ_g^2), and σ_{sg} show the local (3 × 3) estimates of the mean, variance, and covariance respectively, computed for each cell of the two maps S and G. These parameters are defined as follows (Jones et al. 2016):

$$\mu_s = \sum_{j=1}^{n} w_j p_{s_j} \quad (7)$$

$$\sigma_s^2 = \sum_{j=1}^{n} w_j \left(p_{s_j} - \mu_s\right)^2 \quad (8)$$

$$\sigma_{sg} = \sum_{j=1}^{n} w_j \left(p_{s_j} - \mu_s\right)\left(p_{g_j} - \mu_g\right) \quad (9)$$

where p_{s_j} and p_{g_j} indicate the precipitation values for the jth cell in the local window of the maps S and G, respectively. The weight for the 9 cells in the local window, $w_j = 1/9$. The SSI is the product of the three components (i.e. similarity in the mean, variance, and covariance) and was estimated using the following equation:

$$\text{SSI}\ (S, G) = [\text{SIM}(S, G)]^{\alpha}.[\text{SIV}(S, G)]^{\beta}.[\text{SIP}(S, G)]^{\gamma} \quad (10)$$

where α, β, and γ are used to provide weights for the individual components and can be any value greater than zero (i.e. $\alpha > 0$, $\beta > 0$, and $\gamma > 0$). In the current analysis, default values of these three parameters were used i.e. $\alpha = 1$, $\beta = 1$, and $\gamma = 1$. Equation (10) conforms to the following criteria (Jones et al. 2016):

(a) Symmetry: $\text{SSI}\ (S, G) = \text{SSI}\ (G, S)$;

(b) Boundedness: $-1 \leq \text{SSI}\ (S, G) \leq 1$; and

(c) Unique maximum: $\text{SSI}\ (S, G) = 1$, if $S = G$.

It is worth noting that SIM, SIV, and SIP are all evaluated locally. Thus, values of these similarity indices can be presented as maps as well, and the areal extent of the similarity maps is reduced somewhat compared to the original precipitation maps depending on the window size, i.e. 3 × 3 for this study. The similarity indices examined here have the following ranges (Jones et al. 2016, Wiederholt et al. 2019):

SSI varies from -1 (complete dissimilarity between two maps) to +1 (complete similarity between two maps). SIM ranges between 0 (most dissimilar in the mean) and +1 (most similar in the mean). SIV also ranges from 0 (most dissimilar in spatial

variability) to +1 (most similar in spatial variability). SIP varies between -1 (negative correlation i.e. low values of one map correspond to high values in the other) and +1 (positive correlation i.e. low or high values occur in the same area for both maps). SIP value of 0 indicates that there is no correlation between the two maps i.e. the distribution of the cell values is independent of one another.

4. Results and discussion

4.1. Spatial distribution of BR

Figure 2 shows the spatial distribution of BR in the SPPs with respect to SILO dataset over Australia. All these five SPPs overestimate daily precipitation values (BR > 1.20) mostly over the arid zone, while PERSIANN also exhibits overestimation over the northern and north-western regions in summer dominant zone. The overestimation by IMERG, TMPA, CMORPH, PERSIANN, and PERSIANN-CDR consist of 28%, 20%, 25%, 27%, and 30% of analysis grid pixels, respectively. Sub-cloud evaporation, precipitation suppression by desert dusts, and surface misclassification by PMW sensors may be the key factors in overestimation of precipitation over the semi-arid and arid regions by the SPPs (Dinku et al. 2010a). Further, Dinku et al. (2010b) have reported that PERSIANN shows pronounced overestimation for the daily precipitation totals over tropical regions of Colombia.

In contrast, PERSIANN indicates serious underestimation (BR < 0.60) along the western, south-western, south-eastern, and eastern coasts and over TAS (Figure 2). TMPA, CMORPH, and PERSIANN-CDR also underestimate precipitation values for several analysis grid pixels over mountainous tropical east coast of QLD and mountainous western TAS whereas the underestimation is less extensive for IMERG. For PERSIANN, around 32% of the analysis grid boxes are below 0.80, while the

corresponding figures for IMERG, TMPA, CMORPH, and PERSIANN-CDR are only 2%, 5%, 13%, and 4%, respectively. The underestimation along the coasts and over mountainous regions may be associated with warm orographic rain processes (Islam 2018).

All-Australia mean and STD of BR of the SPPs are also shown in Figure 2. TMPA shows the lowest (1.15) all-Australia mean BR, while PERSIANN denotes the highest (1.47). Among the five SPPs, PERSIANN is the only product that does not incorporate any gauge-based bias correction in the precipitation estimation process. The implementation of gauge-based correction notably reduces the overestimation in the IMERG, TMPA, CMORPH, and PERSIANN-CDR datasets. It might be assumed that the extreme overestimation in PERSIANN in central and north-western Australia is compensated by severe underestimation mostly in coastal regions during the computation of all-Australia mean BR. That is why the Z value based on Equation (3) was used to compute all-Australia mean and STD of BR of the SPPs for the purpose of ranking and assessment.

Histograms of BR for the five SPPs are presented in Figure 3 to show the variation in BR values over Australia. For all the SPPs, the majority of grid boxes (81% - 98%) have BR values in the range between 0.50 and 1.50. A small number of pixels is found beyond this range of BR for most of the SPPs, except for PERSIANN for which 19% of grid cells have BR values greater than 1.50 or less than 0.50. This is substantially higher than those for the other products. The frequency distribution of BR shows an interesting feature for IMERG and PERSIANN-CDR. For these two products, the larger proportion of analysis grid boxes (83% and 76%, respectively) has BR greater than one. However, TMPA has the highest number of pixels (48%) with BR in the range

0.90 to 1.10. These results are in good agreement with the findings based on Figure 2 for the study period.

4.2. CC

The spatial distribution of the correlation coefficient (CC) between the five SPPs and the gauge-based SILO dataset is shown in Figure 4. IMERG shows the largest positive correlation across the country except over some regions of WA and SA, followed by TMPA, CMORPH, and PERSIANN-CDR, whereas PERSIANN exhibits the poorest skill. IMERG, TMPA, CMORPH, PERSIANN, and PERSIANN-CDR have CC scores above 0.60 for nearly 93%, 75%, 68%, 19%, and 50% of analysis grid pixels, respectively. TMPA has lower CC values along the southern coast and over western TAS in winter precipitation zone. PERSIANN and PERSIANN-CDR show relatively better performance over the northern Australia in tropical summer precipitation regimes, while both products perform poorly over the southern Australia in winter precipitation regimes. This is particularly true for IR based products. However, gauge-based corrections in the PERSIANN-CDR product contribute to the improvement over IR-only PERSIANN product.

In tropical summer region, the precipitation systems are mostly convective (Ebert et al. 2007). In case of heavy convective precipitation events, both PMW and IR sensors have strong correlation with precipitation (Moazami et al. 2013). Moreover, IR sensors correlate cloud brightness temperature with surface precipitation rate without considering the amount of water available in the cloud. This could lead to the poor performance of PERSIANN in the tropical climate when little water is available in the cloud (Moazami et al. 2013). In comparison, majority of the precipitation in winter is stratiform associated with synoptic systems i.e. frontal systems and cut-off lows. Both

PMW and IR sensors have problems with detecting precipitation from these non-convective clouds in winter (Ebert et al. 2007). Further, the snow cover, specially over mountainous areas, are misidentified as rain by PMW sensors (Ebert et al. 2007).

Figure 5 presents the histograms of CC values for the five SPPs. IMERG clearly performs better than the other products over Australia, followed by TMPA, CMORPH, and PERSIANN-CDR, while PERSIANN shows the lowest correlation with ground-based SILO product by comparison. For IMERG, a large number of grid pixels (more than 37%) has a CC value greater than 0.80, while all the pixels of PERSIANN (100%) have a CC value less than 0.80.

4.3. SSI

SIM, SIV, SIP, and SSI scores for the mean annual precipitation of the five SPPs relative to the SILO data for the study period are shown in Figures 6 and 7. SIM panels of IMERG, TMPA, CMORPH, and PERSIANN-CDR and SIV panels of IMERG and TMPA are not shown here as these metrics do not show much variation for these products (i.e. most of the pixel values of these panels are close to +1). For all the products, except PERSIANN, the local means of the SPPs are comparable with the local means of SILO across the country (SIM close to +1). PERSIANN shows some discrepancy over south-western WA and western TAS (see Figure 6(a)). As seen in Figure 6(c), larger differences in local variance are evident for PERSIANN as compared to SILO (SIV close to 0). CMORPH and PERSIANN-CDR also exhibit dissimilarities in variance over specific regions (see Figure 6(b) and 6(d)) whereas the differences are lower for IMERG and TMPA (not shown here). Although, PERSIANN-CDR has similar local means in comparison with SILO over the western TAS (SIM close to +1, not shown here), it displays larger differences in local variance over this region (see

Figure 6(d)). The reason behind this discrepancy is that SILO shows extremely high mean annual precipitation (> 1500 mm), while the mean annual precipitation of PERSIANN-CDR is close to being uniformly distributed (around 1400 mm). For CMORPH, some isolated grid pixels have higher variations over the arid region (see Figure 6(b)). CMORPH-based mean annual precipitation amounts were quite high for these pixels (> 200 mm) whereas SILO exhibits almost an identical mean annual precipitation of 150 mm. The areas with SIP scores close to +1 indicate the local regions where spatial structure between SILO and the SPP is similar (see Figure 6(e)-(i)). It depicts that pixels with relatively high and low variance are in the same locations of the two maps being compared. Pixels with SIP close to -1 are areas where local spatial structure is dissimilar, pointing to the different spatial pattern in each underlying map. Comparing Figure 6(e)-(i), IMERG and TMPA look better than the other three products. CMORPH shows relatively lower SIP values throughout the country. PERSIANN and PERSIANN-CDR have very dissimilar spatial structure ($-1 < SIP < 0$) particularly over the Snowy mountains in south-eastern region of Australia and TAS.

Figure 7 presents the SSI of the five SPPs, which is the product of the three metrics SIM, SIV, and SIP. Except for PERSIANN, SIV and SIP are the main components contributing to the dissimilarities in spatial structure between SPP and SILO over Australia, while SIM is an additional component for PERSIANN. The SSI scores indicate that satellite precipitation estimation algorithms are not fully able to capture the underlying processes that underpin the spatial patterns of the mean annual precipitation over some regions of Australia. For the products, the means of SSI are also shown for Australia, ranging from 0.81 for PERSIANN to 0.92 for IMERG, indicating high level of similarity in terms of the spatial structure between the five SPPs and SILO with respect to the mean annual precipitation.

4.4. Ranking of SPPs

Table 2 presents the ranking of the SPPs based on a number of skill indicators. Rank 1 indicates the best performing product whereas rank 5 that with the poorest skill. Comparing the total ranking points, IMERG stands out as having the best statistics while PERSIANN is the worst. TMPA is nearly as good as IMERG and the performance of CMORPH is comparable with PERSIANN-CDR. CMORPH, PERSIANN, and PERSIANN-CDR will not be considered further in this analysis because of their relatively poor performance.

4.5. Seasonal SPP skills

4.5.1. BR

In order to investigate the seasonal performance, skill indicators were computed for summer (November-April) and winter (May-October) season over Australia. Figure 8 shows the bias ratio of IMERG and TMPA as compared to SILO in summer and winter for the 5-year study period. IMERG and TMPA have reasonably good skills in estimating the amount of precipitation across the country over summer months, even though both products exhibit overestimation in the dry region. Further, overestimation of precipitation with IMERG is more pronounced than TMPA in winter precipitation zones in summer half of the year, e.g. the southwestern region of Australia. Interestingly for both products, the overestimation becomes more prominent over summer dominant tropical region during cold season. Precipitation occurs infrequently in winter in the tropical northern Australia, and it is associated with either midlatitude frontal systems or orographic uplifting of moist air along the northeast coast. Ebert et al. (2007) have reported that both PMW and IR sensors are unable to capture the tropical wintertime

precipitation. TMPA also underestimates the precipitation values in winter throughout the country, with severe underestimation over western TAS. This underestimation may be attributed to the climatological calibration implemented in the TMPA processing algorithm from October 2014 onward. The second reason is that the nominal coverage of TMI and PR of TRMM satellite was 38° N-S (Yong et al. 2013). The calibration beyond this latitude band is simply taken as it is just Equatorward of 40° for both hemispheres due to the absence of TCI data to use as the reference (Huffman et al. 2010). In general, the climatological calibration improves TMPA precipitation estimates in summer, while poorer performances were observed for high latitudes, predominantly in winter. This finding was consistent with the result obtained by Yong et al. (2013).

4.5.2. CC

Figure 9 shows the performances of IMERG and TMPA to capture the temporal behaviour of observed summer and winter precipitation. In terms of CC, IMERG outperformed TMPA across the country in summer. However, the CC values for both SPPs were much lower over some parts of arid region. IMERG indicates improved performance to detect winter precipitation with little discrepancy in the summer dominant tropical region. Conversely, the performance of TMPA was relatively poor during cold season, although it performed better in eastern Australia. The improved performance of IMERG compared to its predecessor TMPA was associated with the most advanced sensors i.e. GPM Microwave Imager (GMI) and Dual-frequency Precipitation Radar (DPR). These sensors have excellent capability in detecting very light as well as heavy precipitation events (Hou et al. 2014).

4.5.3. SSI

SSI metric to show the similarity in the spatial pattern of the mean seasonal precipitation based on IMERG and TMPA in comparison with the mean seasonal SILO data is presented in Figure 10. SIM, SIV, and SIP panels of IMERG and TMPA are not presented here as these metrics do not show much variation (i.e. most of the pixel values are close to +1). The performance of IMERG during winter appears to be better than TMPA. For the two products, differences in the spatial structure of the mean seasonal precipitation are found essentially in the northern Australia in summer, while these differences are common in the southern Australia in winter. Moreover, IMERG and TMPA show greater dissimilarities along the southern coast and in TAS, respectively in summer, whereas both products show poor performance over mountainous east coast of QLD in winter. For TMPA, some isolated areas also have lower SSI values in arid zone in winter.

5. Conclusions

In this study, the latest version of five SPPs i.e. IMERG, TMPA, CMORPH, PERSIANN, and PERSIANN-CDR were evaluated against gauge-based gridded SILO dataset in Australia for the period from October 2014 to September 2019. The analysis was performed at daily, seasonal, and annual time scales. Bias ratio and linear correlation coefficient for Australia showed that IMERG and TMPA performed better than CMORPH, PERSIANN, and PERSIANN-CDR when compared with ground-based SILO data. According to the seasonal statistics, IMERG indicated relatively better performance in winter, although the BR and CC values were not so good over the summer dominant tropical region during this season. On the other hand, TMPA showed poorer skill in winter. Overall, IMERG stood out as the best product for Australia. The

performance of TMPA was also promising, considering the climatological calibration applied in the precipitation estimation algorithm from October 2014 due to the absence of TCI data. When all data were included in the analysis, the BR values of TMPA were better than those of IMERG. Further, TMPA had an advantage of IMERG in terms of seasonal BR in summer.

The SSI metric was applied for the first time to compare a pair of gridded mean annual precipitation maps. An advantage of the SSI method is that SIM, SIV, and SIP were calculated to show similarities between the two underlying maps which could not be seen simply through visual inspection. The SSI map was computed by multiplying the SIM, SIV, and SIP maps, and the mean of the estimated SSI values for the map could be used as a simple but effective skill indicator. The SSI scores showed that all the SPPs had dissimilarities with ground-based SILO product in terms of the spatial pattern of the mean annual precipitation, particularly over some high precipitation regions. SIM, SIV, and SIP metrics revealed the local scale differences in the mean, variance, and covariance between the pair of maps being compared whereas these differences were not visible in conventional map comparison technique, for instance, cell by cell comparison applied in this study to estimate BR and CC.

IR-only PERSIANN had the poorest skills around Australia, which was evident from the extremely high and low BR and lower CC values. For instance, BR was greater than 1.50 or less than 0.50 for almost 19% of the land surface in Australia. PERSIANN also had CC values less than 0.60 for approximate 81% of the land surface. However, bias-corrected PERSIANN-CDR showed better performance in the tropics where most precipitation occurs in summer. Despite the serious under- and overestimation in places, CMORPH indicated reasonable daily precipitation detection skills. The results pointed

to the fact that the current bias adjustment techniques of PERSIANN-CDR and CMORPH did not effectively reduce the biases of these two products in Australia.

6. Acknowledgements

The first author acknowledges Griffith University, Queensland, Australia for providing financial support through GUIPRS and GUPRS scholarships. The authors would like to thank the two anonymous reviewers for their constructive comments and suggestions which bring substantial improvement in the revised version of the manuscript.

7. References

Adler, R. F., *et al.*, 2003. The version-2 global precipitation climatology project (GPCP) monthly precipitation analysis (1979-present). *Journal of Hydrometeorology,* 4(6), 1147-1167. doi:10.1175/1525-7541(2003)004<1147:Tvgpcp>2.0.Co;2

Ashouri, H., *et al.*, 2015. PERSIANN-CDR: Daily precipitation climate data record from multisatellite observations for hydrological and climate studies. *Bulletin of the American Meteorological Society,* 96(1), 69-83. doi:10.1175/BAMS-D-13-00068.1

Braun, S., *et al.*, 2014. *TRMM Precipitation Radar data suspended*. Available from: https://gpm.nasa.gov/mission-updates/gpm-news/trmm-precipitation-radar-data-suspended [Accessed 25 June 2020].

Brunetti, M. T., *et al.*, 2018. How far are we from the use of satellite rainfall products in landslide forecasting? *Remote Sensing of Environment,* 210, 65-75. doi:10.1016/j.rse.2018.03.016

Bureau of Meteorology, 2020. *Optimal radar coverage areas*. Available from: http://www.bom.gov.au/australia/radar/about/radar_coverage_national.shtml [Accessed 8 April 2020].

Chappell, A., *et al.*, 2013. Evaluating geostatistical methods of blending satellite and gauge data to estimate near real-time daily rainfall for Australia. *Journal of Hydrology,* 493, 105-114. doi:10.1016/j.jhydrol.2013.04.024

Chen, Y. J., *et al.*, 2013. Evaluation of TMPA 3B42 daily precipitation estimates of tropical cyclone rainfall over Australia. *Journal of Geophysical Research: Atmospheres,* 118(21), 11966-11978. doi:10.1002/2013JD020319

Dinku, T., *et al.*, 2010a. Evaluating Detection Skills of Satellite Rainfall Estimates over Desert Locust Recession Regions. *Journal of Applied Meteorology and Climatology,* 49(6), 1322-1332. doi:10.1175/2010jamc2281.1

Dinku, T., *et al.*, 2010b. Validation and Intercomparison of Satellite Rainfall Estimates over Colombia. *Journal of Applied Meteorology and Climatology,* 49(5), 1004-1014. doi:10.1175/2009jamc2260.1

Ebert, E. E., Janowiak, J. E. and Kidd, C., 2007. Comparison of near-real-time precipitation estimates from satellite observations and numerical models. *Bulletin of the American Meteorological Society,* 88(1), 47-64. doi:10.1175/BAMS-88-1-47

Grose, M. R., *et al.*, 2013. A regional response in mean westerly circulation and rainfall to projected climate warming over Tasmania, Australia. *Climate Dynamics,* 40(7-8), 2035-2048. doi:10.1007/s00382-012-1405-1

Hong, Y., *et al.*, 2004. Precipitation Estimation from Remotely Sensed Imagery using an Artificial Neural Network Cloud Classification System. *Journal of Applied Meteorology,* 43(12), 1834-1852. doi:10.1175/Jam2173.1

Hou, A. Y., *et al.*, 2014. The Global Precipitation Measurement Mission. *Bulletin of the American Meteorological Society,* 95(5), 701-722. doi:10.1175/BAMS-D-13-00164.1

Hsu, K. L.*, et al.*, 1997. Precipitation estimation from remotely sensed information using artificial neural networks. *Journal of Applied Meteorology,* 36(9), 1176-1190. doi:10.1175/1520-0450(1997)036<1176:Pefrsi>2.0.Co;2

Huffman, G. J.*, et al.*, 2010. The TRMM Multi-Satellite Precipitation Analysis (TMPA). *In:* Gebremichael, M. and Hossain, F. eds. *Satellite Rainfall Applications for Surface Hydrology.* Dordrecht: Springer Netherlands, 3-22. doi:10.1007/978-90-481-2915-7_1

Huffman, G. J.*, et al.*, 2020. Integrated Multi-satellite Retrievals for the Global Precipitation Measurement (GPM) Mission (IMERG). *In:* Levizzani, V.*, et al.* eds. *Satellite Precipitation Measurement: Volume 1.* Cham: Springer International Publishing, 343-353. doi:10.1007/978-3-030-24568-9_19

Huffman, G. J.*, et al.*, 2007. The TRMM Multisatellite Precipitation Analysis (TMPA): Quasi-global, multiyear, combined-sensor precipitation estimates at fine scales. *Journal of Hydrometeorology,* 8(1), 38-55. doi:10.1175/jhm560.1

Huffman, G. J.*, et al.*, 2019. *GPM IMERG Final Precipitation L3 Half Hourly 0.1 degree x 0.1 degree V06.* Greenbelt, MD: Goddard Earth Sciences Data and Information Services Center (GES DISC) [Accessed 20 March 2020]. doi:10.5067/GPM/IMERG/3B-HH/06

Islam, M. A., 2018. Statistical comparison of satellite-retrieved precipitation products with rain gauge observations over Bangladesh. *International Journal of Remote Sensing,* 39(9), 2906-2936. doi:10.1080/01431161.2018.1433890

Jeffrey, S. J.*, et al.*, 2001. Using spatial interpolation to construct a comprehensive archive of Australian climate data. *Environmental Modelling & Software,* 16(4), 309-330. doi:10.1016/S1364-8152(01)00008-1

Jones, D. A., Wang, W. and Fawcett, R., 2009. High-quality spatial climate data-sets for Australia. *Australian Meteorological and Oceanographic Journal,* 58(4), 233-248. doi:10.22499/2.5804.003

Jones, E. L.*, et al.*, 2016. Novel application of a quantitative spatial comparison tool to species distribution data. *Ecological Indicators,* 70, 67-76. doi:10.1016/j.ecolind.2016.05.051

Joyce, R. J.*, et al.*, 2004. CMORPH: A method that produces global precipitation estimates from passive microwave and infrared data at high spatial and temporal resolution. *Journal of Hydrometeorology,* 5(3), 487-503. doi:10.1175/1525-7541(2004)005<0487:Camtpg>2.0.Co;2

Joyce, R. J. and Xie, P. P., 2011. Kalman Filter-Based CMORPH. *Journal of Hydrometeorology,* 12(6), 1547-1563. doi:10.1175/Jhm-D-11-022.1

King, A. D.*, et al.*, 2014. Extreme rainfall variability in Australia: Patterns, drivers, and predictability. *Journal of Climate,* 27(15), 6035-6050. doi:10.1175/Jcli-D-13-00715.1

Li, M. and Shao, Q., 2010. An improved statistical approach to merge satellite rainfall estimates and raingauge data. *Journal of Hydrology,* 385(1), 51-64. doi:10.1016/j.jhydrol.2010.01.023

Li, Z.*, et al.*, 2015. Multiscale hydrologic applications of the latest satellite precipitation products in the Yangtze river basin using a distributed hydrologic model. *Journal of Hydrometeorology,* 16(1), 407-426. doi:10.1175/Jhm-D-14-0105.1

Maggioni, V., Meyers, P. C. and Robinson, M. D., 2016. A review of merged high-resolution satellite precipitation product accuracy during the Tropical Rainfall Measuring Mission (TRMM) era. *Journal of Hydrometeorology,* 17(4), 1101-1117. doi:10.1175/Jhm-D-15-0190.1

Maher, P. and Sherwood, S. C., 2014. Disentangling the multiple sources of large-scale variability in Australian wintertime precipitation. *Journal of Climate,* 27(17), 6377-6392. doi:10.1175/Jcli-D-13-00659.1

Mei, Y. W.*, et al.*, 2014. Error analysis of satellite precipitation products in mountainous basins. *Journal of Hydrometeorology,* 15(5), 1778-1793. doi:10.1175/Jhm-D-13-0194.1

Moazami, S.*, et al.*, 2013. Comparison of PERSIANN and V7 TRMM Multi-satellite Precipitation Analysis (TMPA) products with rain gauge data over Iran. *International Journal of Remote Sensing,* 34(22), 8156-8171. doi:10.1080/01431161.2013.833360

Nicholls, N., Drosdowsky, W. and Lavery, B., 1997. Australian rainfall variability and change. *Weather,* 52(3), 66-72. doi:10.1002/j.1477-8696.1997.tb06274.x

Peña-Arancibia, J. L.*, et al.*, 2013. Evaluation of precipitation estimation accuracy in reanalyses, satellite products, and an ensemble method for regions in Australia and south and east Asia. *Journal of Hydrometeorology,* 14(4), 1323-1333. doi:10.1175/Jhm-D-12-0132.1

Pipunic, R. C.*, et al.*, 2013. Evaluation of real-time satellite precipitation products in semi arid/arid Australia. ed. *20th International Congress on Modelling and Simulation, MODSIM2013*, 2013 Adelaide, Australia, 3106-3112.

Pipunic, R. C.*, et al.*, 2015. An evaluation and regional error modeling methodology for near-real-time satellite rainfall data over Australia. *Journal of Geophysical Research: Atmospheres,* 120(20), 10767-10783. doi:10.1002/2015jd023512

Prosser, I. P., 2011. Current water availability and use. *In:* Prosser, I. P. ed. *Water: Science and solutions for Australia.* Collingwood, Victoria: CSIRO, 1-16.

Risbey, J. S.*, et al.*, 2009. On the remote drivers of rainfall variability in Australia. *Monthly Weather Review,* 137(10), 3233-3253. doi:10.1175/2009mwr2861.1

Rossi, M.*, et al.*, 2017. Statistical approaches for the definition of landslide rainfall thresholds and their uncertainty using rain gauge and satellite data. *Geomorphology,* 285, 16-27. doi:10.1016/j.geomorph.2017.02.001

Schuster, G.*, et al.*, 2011. Application of satellite precipitation data to analyse and model arbovirus activity in the tropics. *International Journal of Health Geographics,* 10. doi:10.1186/1476-072x-10-8

Sewell, T.*, et al.*, 2016. Disaster declarations associated with bushfires, floods and storms in New South Wales, Australia between 2004 and 2014. *Scientific Reports,* 6. doi:10.1038/srep36369

Sivakumar, B., Woldemeskel, F. M. and Puente, C. E., 2014. Nonlinear analysis of rainfall variability in Australia. *Stochastic Environmental Research and Risk Assessment,* 28(1), 17-27. doi:10.1007/s00477-013-0689-y

Sorooshian, S.*, et al.*, 2000. Evaluation of PERSIANN system satellite-based estimates of tropical rainfall. *Bulletin of the American Meteorological Society,* 81(9), 2035-2046. doi:10.1175/1520-0477(2000)081<2035:Eopsse>2.3.Co;2

Tan, J.*, et al.*, 2019. IMERG V06: Changes to the morphing algorithm. *Journal of Atmospheric and Oceanic Technology,* 36(12), 2471-2482. doi:10.1175/Jtech-D-19-0114.1

Tan, M. L. and Santo, H., 2018. Comparison of GPM IMERG, TMPA 3B42 and PERSIANN-CDR satellite precipitation products over Malaysia. *Atmospheric Research,* 202, 63-76. doi:10.1016/j.atmosres.2017.11.006

Tang, G.*, et al.*, 2016. Statistical and hydrological comparisons between TRMM and GPM level-3 products over a midlatitude basin: Is day-1 IMERG a good

successor for TMPA 3B42V7? *Journal of Hydrometeorology,* 17(1), 121-137. doi:10.1175/jhm-d-15-0059.1

Vernimmen, R. R. E.*, et al.*, 2012. Evaluation and bias correction of satellite rainfall data for drought monitoring in Indonesia. *Hydrology and Earth System Sciences,* 16(1), 133-146. doi:10.5194/hess-16-133-2012

Wang, Z.*, et al.*, 2004. Image quality assessment: From error visibility to structural similarity. *Ieee Transactions on Image Processing,* 13(4), 600-612. doi:10.1109/Tip.2003.819861

Wiederholt, R.*, et al.*, 2019. A multi-indicator spatial similarity approach for evaluating ecological restoration scenarios. *Landscape Ecology,* 34(11), 2557-2574. doi:10.1007/s10980-019-00904-w

Xie, P. P.*, et al.*, 2017. Reprocessed, bias-corrected CMORPH global high-resolution precipitation estimates from 1998. *Journal of Hydrometeorology,* 18(6), 1617-1641. doi:10.1175/Jhm-D-16-0168.1

Xu, R.*, et al.*, 2017. Ground validation of GPM IMERG and TRMM 3B42V7 rainfall products over southern Tibetan Plateau based on a high-density rain gauge network. *Journal of Geophysical Research: Atmospheres,* 122(2), 910-924. doi:10.1002/2016jd025418

Xue, X. W.*, et al.*, 2013. Statistical and hydrological evaluation of TRMM-based multi-satellite precipitation analysis over the Wangchu basin of Bhutan: Are the latest satellite precipitation products 3B42V7 ready for use in ungauged basins? *Journal of Hydrology,* 499, 91-99. doi:10.1016/j.jhydrol.2013.06.042

Yong, B.*, et al.*, 2013. First evaluation of the climatological calibration algorithm in the real- time TMPA precipitation estimates over two basins at high and low latitudes. *Water Resources Research,* 49(5), 2461-2472. doi:10.1002/wrcr.20246

Table 1: Summary of the satellite precipitation products and the SILO reference dataset used in this study.

Products	Spatial resolution (degree)	Time resolution (h)	Sensor type	Gauge-adjusted
IMERG	0.10	0.5	PMW and IR	Yes
TMPA	0.25	3	PMW and IR	Yes
CMORPH	0.25	1	PMW	Yes
PERSIANN	0.25	1	IR	No
PERSIANN-CDR	0.25	24	IR	Yes
SILO	0.05	24	--	--

Table 2: Ranking of the five satellite-based precipitation products according to different quality indicators. Rank of 1 is the best; the lowest in terms of the bias ratio (BR), the highest in terms of the correlation coefficient (CC) and structural similarity index (SSI), and the lowest in terms of the standard deviation (STD) for both BR and CC.

Products	BR		CC		SSI	Total
	Mean	STD†	Mean	STD†		
IMERG	2	1	1	1	1	6
TMPA	1	2	2	2	2	9
PERSIANN-CDR	3	3	4	3	3	16
CMORPH	4	4	3	4	4	19
PERSIANN	5	5	5	5	5	25

†Third decimal place of STD values is used to rank the products if second decimal place has equal numbers.

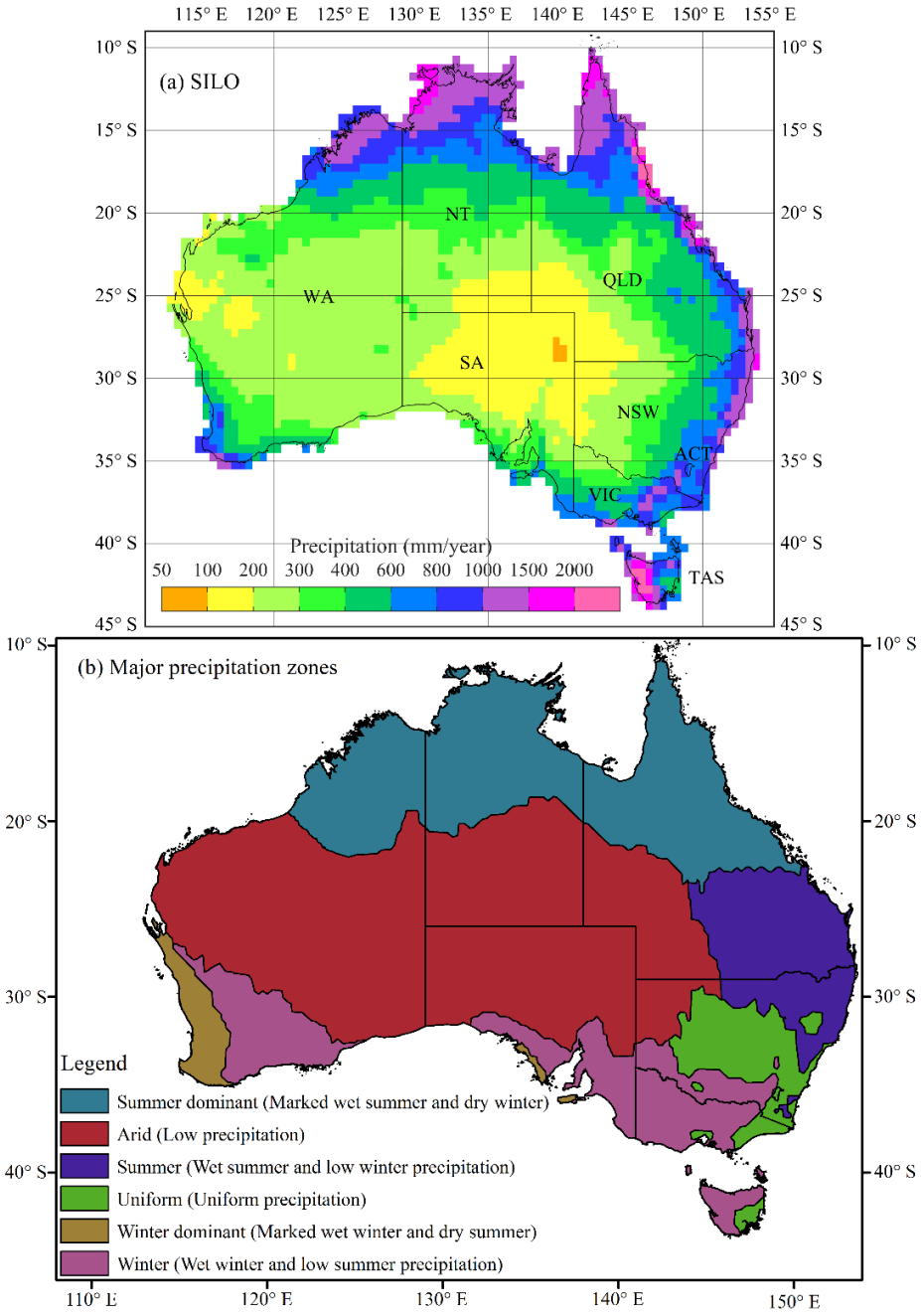

Figure 1. (a) Mean annual precipitation (mm) for the period from October 2014 to September 2019 derived from SILO dataset and (b) major precipitation zones of Australia based on the median (50th percentile) annual precipitation and seasonal incidence. The seasonal incidence is determined from the ratio of the median precipitation values in November to April over that in May to October (source: Bureau of Meteorology).

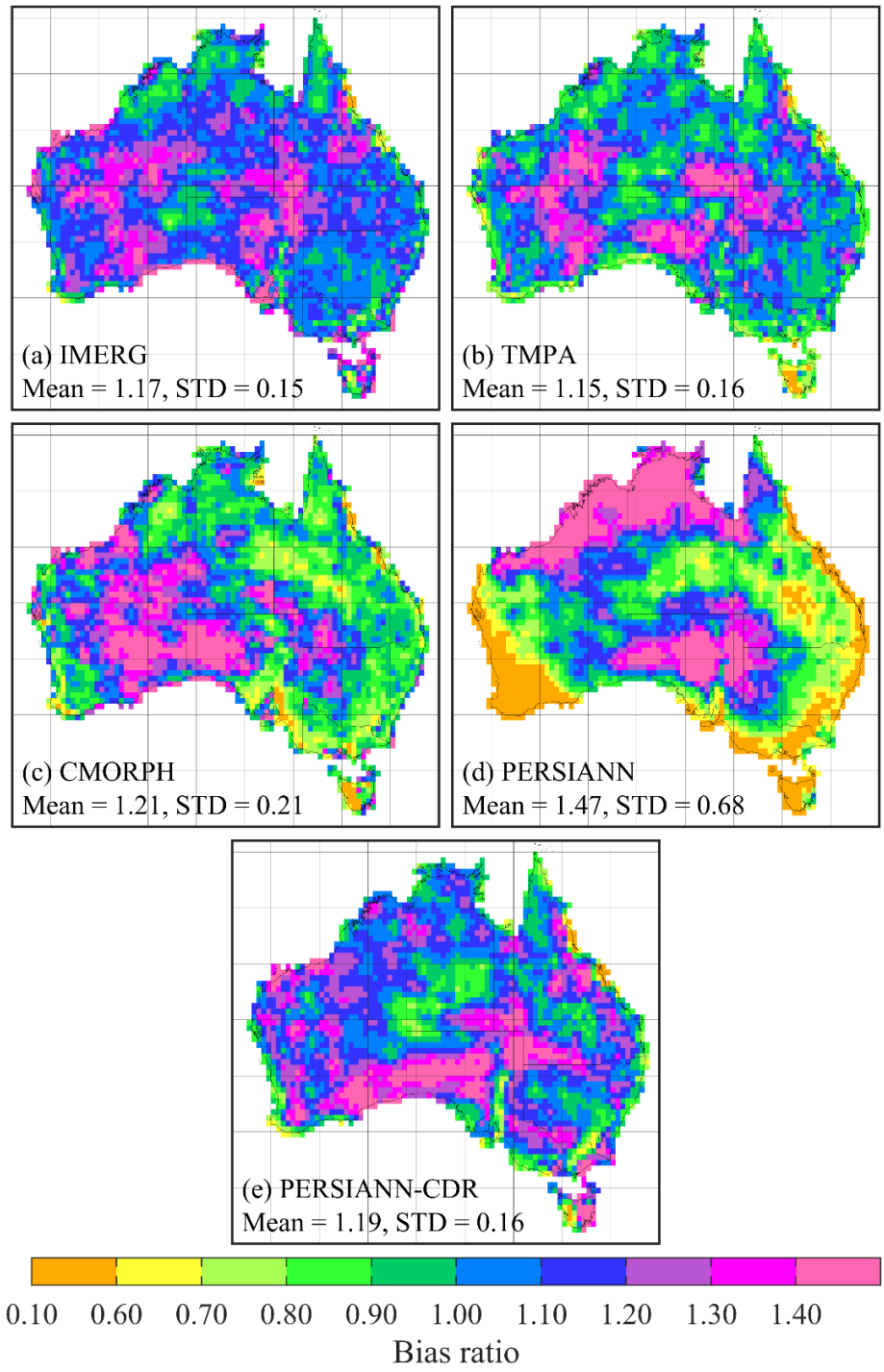

Figure 2. Spatial distribution of the bias ratio for (a) IMERG, (b) TMPA, (c) CMORPH, (d) PERSIANN, and (e) PERSIANN-CDR products relative to gauge-based SILO data for the period from October 2014 to September 2019. The mean and standard deviation of the bias ratio are also shown for each product.

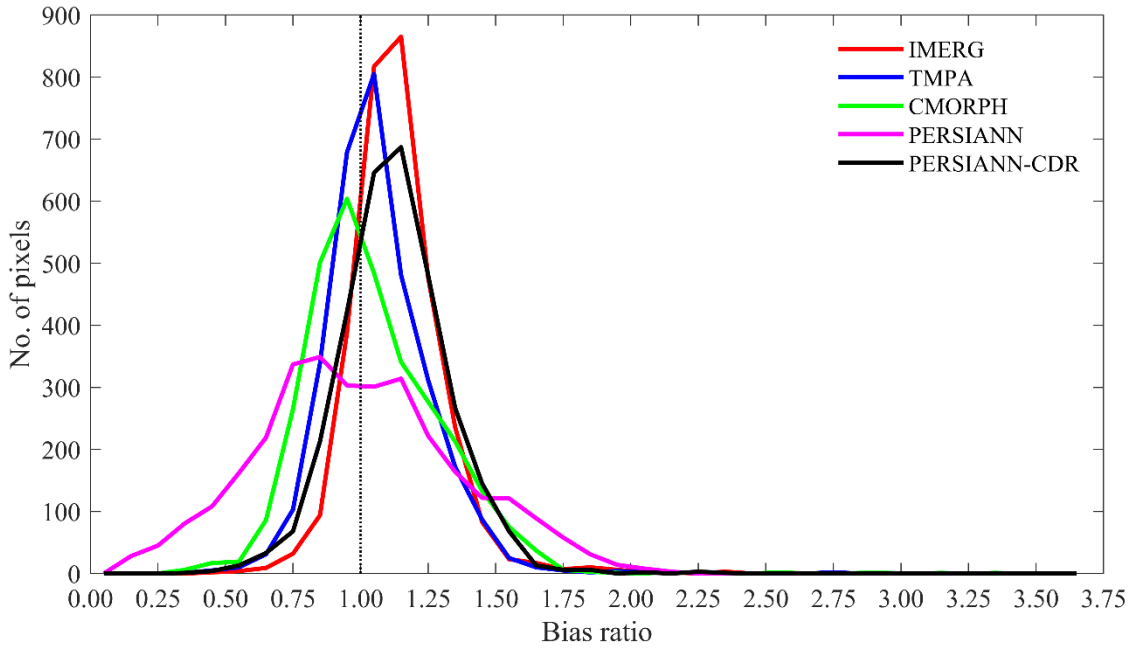

Figure 3. Histograms of the bias ratio derived from IMERG, TMPA, CMORPH, PERSIANN, and PERSIANN-CDR products for Australia for the period from October 2014 to September 2019.

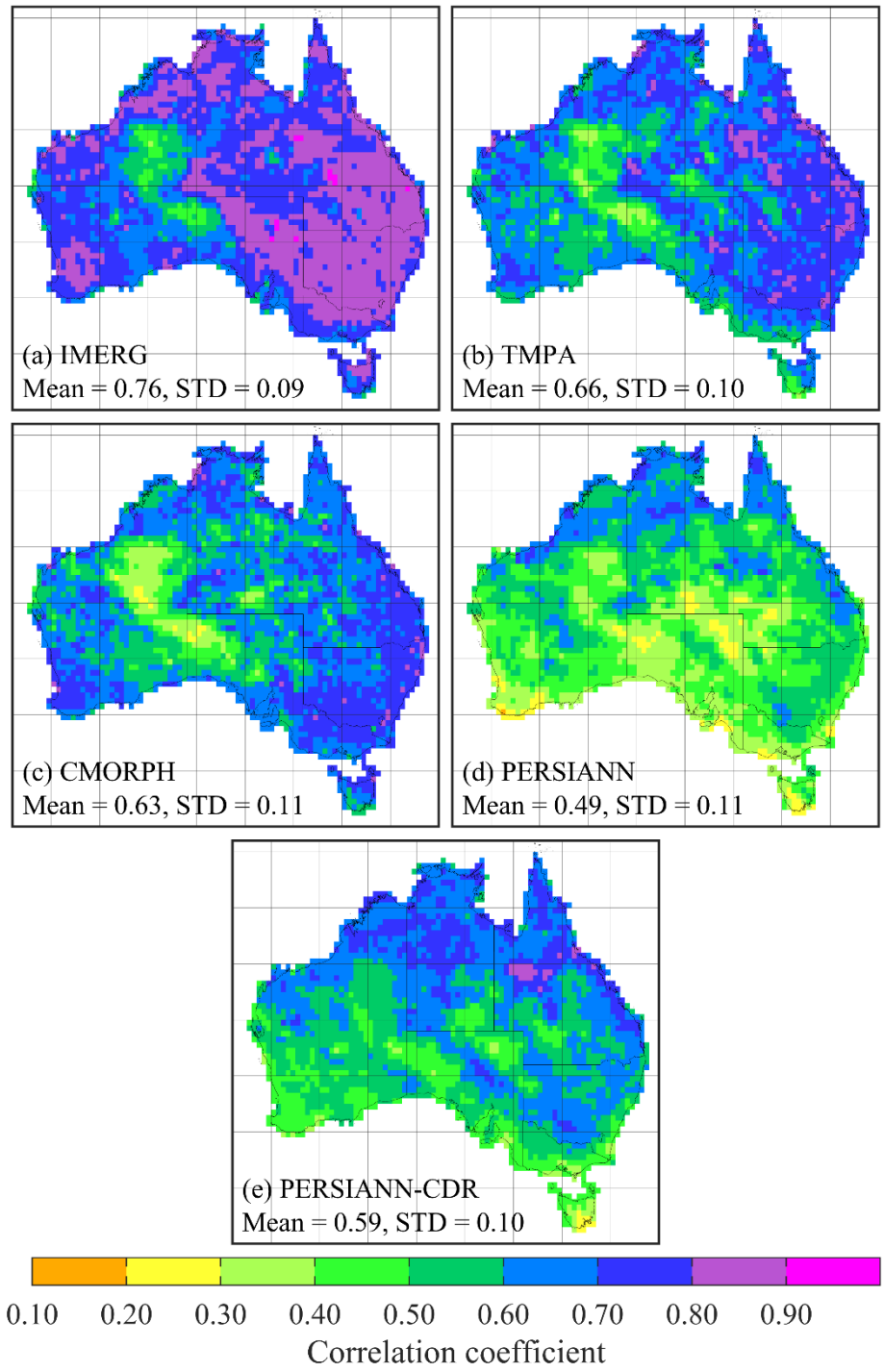

Figure 4. Spatial distribution of the correlation coefficient for the daily precipitation between gauge-based SILO data and (a) IMERG, (b) TMPA, (c) CMORPH, (d) PERSIANN, and (e) PERSIANN-CDR products for the period from October 2014 to September 2019. The mean and standard deviation of the correlation coefficient are also shown for each product.

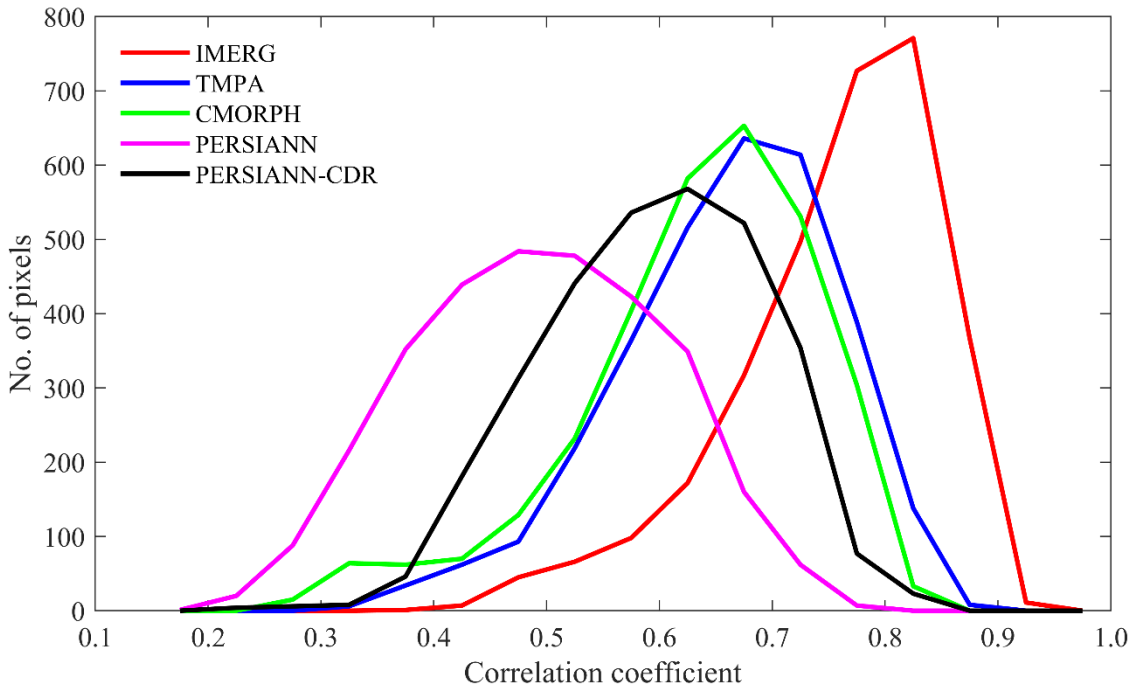

Figure 5. Histograms of the correlation coefficient for the daily precipitation between gauge-based SILO data and IMERG, TMPA, CMORPH, PERSIANN, and PERSIANN-CDR products for Australia for the period from October 2014 to September 2019.

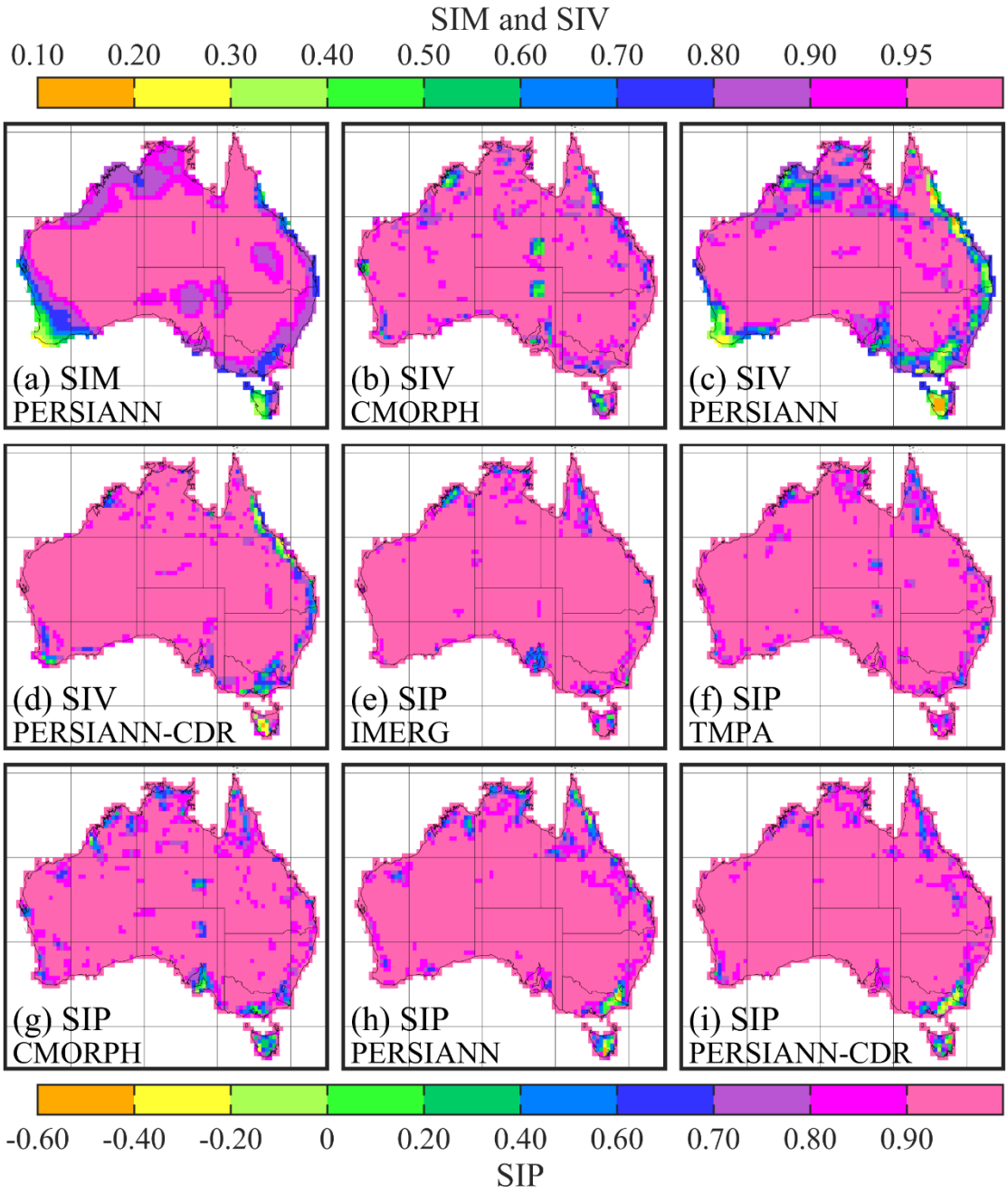

Figure 6. Similarity in the mean annual precipitation between SILO data and the five satellite precipitation products in terms of the mean (SIM) for (a) PERSIANN, the variance (SIV) for (b) CMORPH, (c) PERSIANN, and (d) PERSIANN-CDR, and the pattern of spatial covariance (SIP) for (e) IMERG, (f) TMPA, (g) CMORPH, (h) PERSIANN, and (i) PERSIANN-CDR. Top colorbar is provided for Figure 6(a)-(d), while the bottom one corresponds to Figure 6(e)-(i).

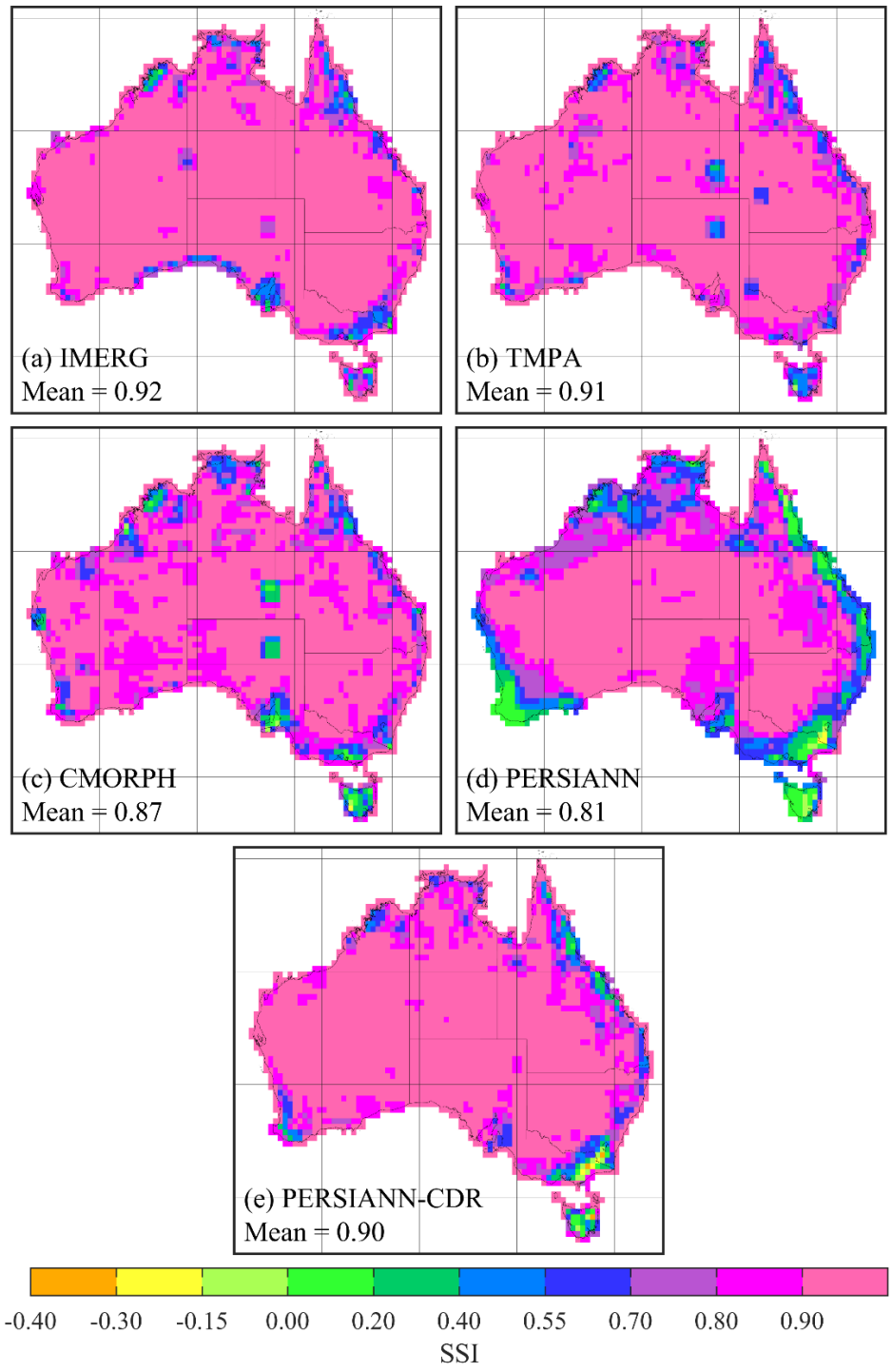

Figure 7. Similarity in the mean annual precipitation between SILO data and the five satellite precipitation products in terms of the structural similarity index (SSI) score for (a) IMERG, (b) TMPA, (c) CMORPH, (d) PERSIANN, and (e) PERSIANN-CDR. The mean SSI score is also shown for each of the five products.

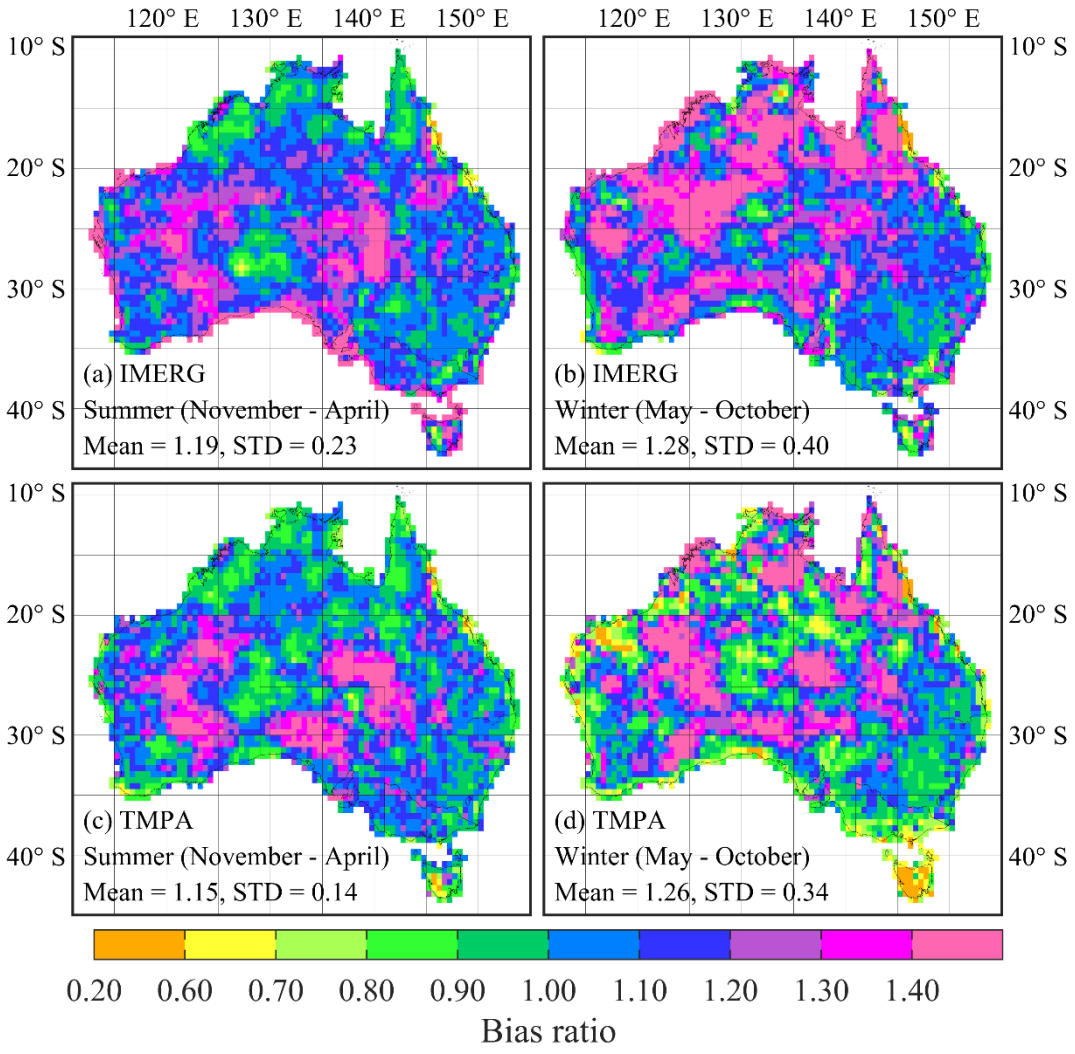

Figure 8. Seasonal distribution of the bias ratio for IMERG and TMPA precipitation products relative to gauge-based SILO data for the period from October 2014 to September 2019. The mean and standard deviation of the bias ratio are also shown for the two products.

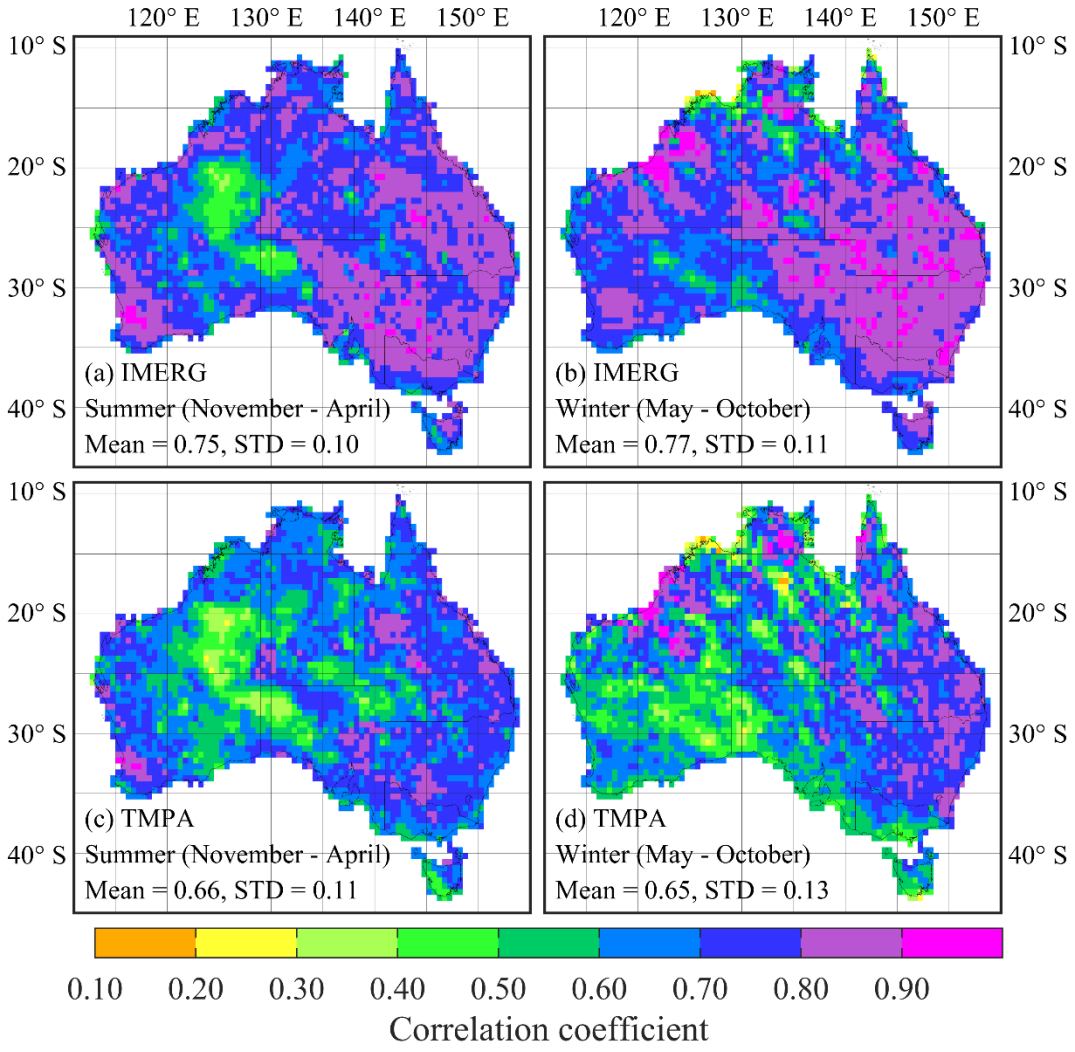

Figure 9. Seasonal distribution of the correlation coefficient for the daily precipitation between gauge-based SILO data and IMERG and TMPA products for Australia for the period from October 2014 to September 2019. The mean and standard deviation (STD) of the correlation coefficient are also shown for the two products.

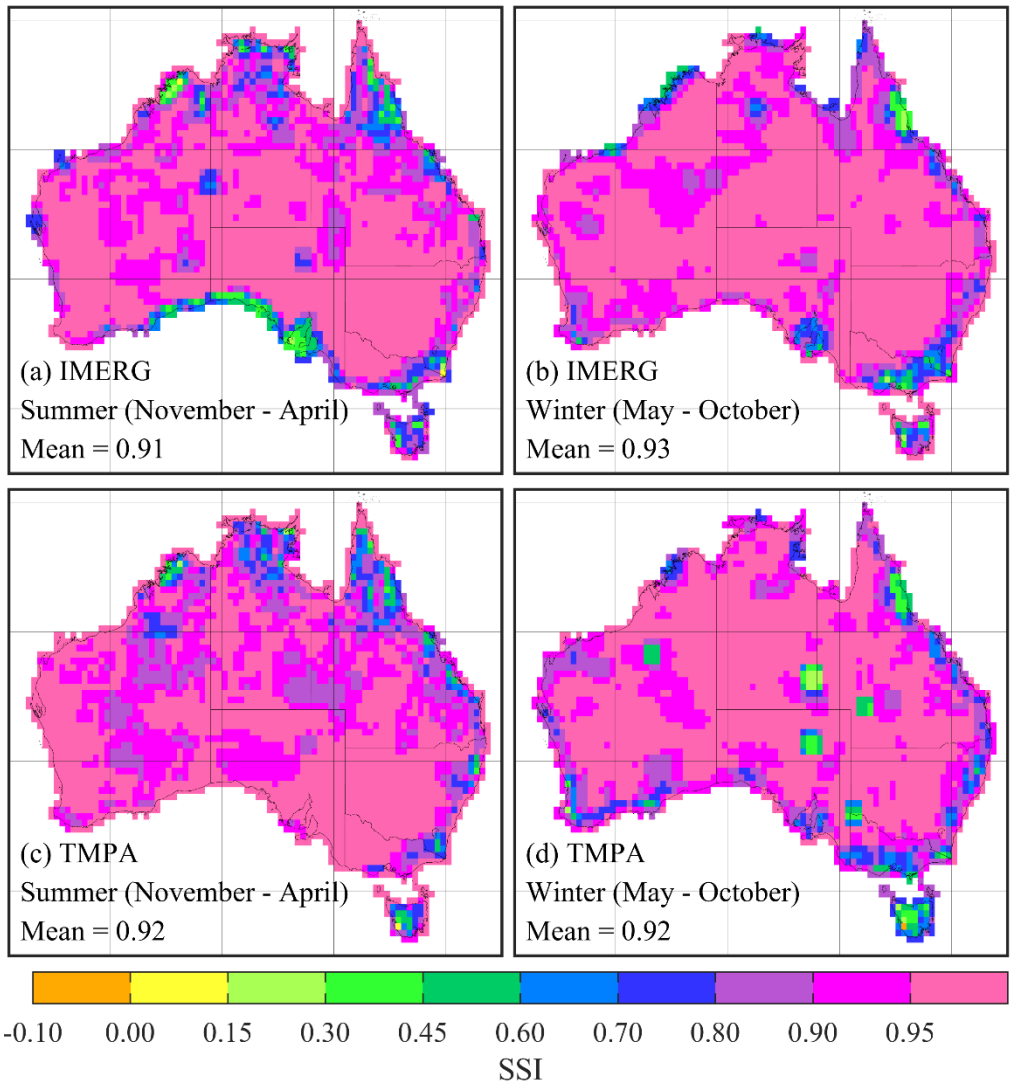

Figure 10. Similarity in the mean seasonal precipitation between SILO data and IMERG and TMPA in terms of the structural similarity index (SSI) score for the period from October 2014 to September 2019. The mean SSI score is also shown for the two products.

Highlights

1. Satellite-based precipitation products evaluated for Australia.
2. Structural Similarity Index applied for the first time to compare the spatial distribution of precipitation.
3. GPM-based IMERG stands out as the best for Australia out of the five products evaluated.
4. TRMM-based TMPA performs reasonably well, considering its climatological calibration.

Declaration of interests

The authors declare that they have no known competing financial interests or personal relationships that could have appeared to influence the work reported in this paper.